DOI 10.24425/aee.2026.158266

Direct equivalent circuit parameter extraction for a brushless doubly-fed induction machine with a nested-loop rotor winding from a finite element model

MARIUSZ JAGIEŁA ✉, MARIAN ŁUKANISZYN, RADOSŁAW WIWATOWSKI

Opole University of Technology
Faculty of Electrical Engineering, Automatic Control and Informatics
76 Prószkowska St, 45-758 Opole

e-mail: {✉ m.jagiela/m.lukaniszyn}@po.edu.pl, r.wiwatowski@student.po.edu.pl

(Received: 21.01.2026, revised: 28.04.2026)

Abstract: The Simplified Equivalent Circuit Model (SECM) is well established as a tool for the performance analysis of the Brushless Doubly-Fed Induction Machine (BDFIM). However, the SECM typically relies on a constant-parameter approximation, which, in theory, contradicts the machine's inherent velocity-dependent nature, given its typical nested-loop rotor structure that couples magnetically with a large portion of the air-gap field harmonics' spectrum. This paper investigates the physics behind this by directly deriving its parameters from rigorous power-balance equations and a time-harmonic finite-element model. The study identifies a self-compensating mechanism: although the extracted rotor leakage reactance and effective turns ratio exhibit significant variations near the natural speed, their combined interaction minimises the impact on terminal quantities. Furthermore, the paper investigates the validity determinants of the constant-parameter SECM in double-feed mode and explains the factors of the conditional accuracy.

Key words: brushless machines, equivalent circuits, finite elements, induction machines, synchronous machines

List of symbols

$\underline{x}$	Complex number
$\underline{x}^*$	Complex conjugate number
ℓ	Axial length
d, q	Direct and quadrature axes
$\Re, \Im$	Real, imaginary part of a complex number
div	Divergence operator
curl	Curl operator
grad	Gradient operator
RMS	Root mean square value
RPM	Revolutions per minute

1. Introduction

Previous research has established the optimal configuration for a brushless doubly-fed induction machine (BDFIM) with a nested-loop rotor winding [1–6]. It is suitable for wind power generation systems [7–9]. The commercial viability of this technology has improved due to clarifying its performance characteristics and resolving the main control-related issues [10,11]. The 2T simplified single-phase steady-state equivalent circuit model (see Fig. 1) [1–5] has been instrumental in driving this progress. The term "simplified" refers to the multi-loop, nested-rotor winding design, which assumes a single loop per nest. In this paper, the model is referred to as the SECM (Simplified Equivalent Circuit Model). Other equivalent circuit models have also been proposed [14]. Efforts have been made to enhance the SECM to address core losses [15, 16], although the fundamental form is considered in this work. A review of equivalent circuit models of BDFIMs presented in the literature, including models of various orders and those that consider or neglect core losses, is provided in [18], along with an assessment of their dynamic performance. All examined models depend on constant equivalent parameters.

Implementing SECMs relies on accurately determining its parameters, which poses a significant challenge. Some studies use the SECM without mentioning the method used to obtain the parameters [12, 16, 17]. The work [19] outlines the following techniques used for this purpose:

i) The parameters are calculated using machine geometry data during the design stage.
ii) The parameters are estimated through curve fitting using data from steady-state measurements of the terminal quantities.
iii) The parameters are obtained from numerical models and experimental tests.

In [20], the rotor winding parameters for the nested-loop design were obtained from the finite element analysis results, although no details were provided about the latter. From the earlier work of the same authors [19], it can be deduced that these parameters were determined, assuming that the loops are connected in parallel and that the impedances of the loops can be calculated separately.

It was recognised that the rotor winding parameters and the effective rotor turns ratio depend on the rotor speed. The results suggest that, from the viewpoint of RMS values of the terminal quantities, this dependence is negligible within a typical operating condition. Two analytical approaches for determining rotor parameters are outlined in reference [21]. Work [22] presents an experimental method that uses only the terminal quantities, thus eliminating the need for complex analytical models. The study formulated equations for the parameters of a modified SECM and conducted tests under both no-load and locked-rotor conditions. The estimated parameters are favourably compared with those obtained through the methods outlined in [19].

Existing methods, while useful, present certain limitations. Analytical techniques can be complex and prone to inaccuracies, while experimental methods require physical prototypes and extensive data processing. Consequently, a precise and direct method applicable at any stage of design is highly desirable. Moreover, relying on terminal measurements and curve-fitting methods can mask local electromagnetic interactions because, to minimise the squared error, the parameters are averaged. The proposed FEM-based approach enables the isolation of specific harmonic effects – such as the impact of differential leakage fluxes on rotor impedance – which are analytically complex and experimentally challenging to separate from other phenomena, like core losses. To address this need, this paper proposes a direct parameter-extraction procedure based on power-balance equations and a time-harmonic finite-element model described in [25, 26]. However, the contribution of this work extends beyond the extraction methodology itself. It aims to investigate the physics underlying equivalent parameters, specifically addressing how a constant-parameter model effectively describes a machine with inherently frequency-dependent rotor parameters. Specifically, this study:

i) Identifies a self-compensating mechanism involving the effective turns ratio varying oppositely to the rotor impedance, which explains the model's accuracy in single-feed operation despite parameter variations.
ii) Identifies the factors affecting the constant-parameter SECM accuracy in double-feed mode in low- and high-power ranges.

The results are applicable to the steady-state operation of a BDFIM with a nested-loop rotor winding.

2. Framework of models

2.1. The SECM

Figure 1 shows the circuit diagram for the SECM and the nested-loop rotor winding of a physical BDFIM.

There are two fundamental frequencies for the stator windings: ω_p for the power winding and ω_c for the control winding, and two rotor slips: s_p, relative to the power winding, and s_c, relative to the control winding:

$$s_p = \frac{\omega_p - p_p \omega_r}{\omega_p}, \tag{1}$$

$$s_c = \frac{\omega_c - p_c \omega_r}{\omega_c}. \tag{2}$$

p_p and p_c are the power winding and control winding pole-pair numbers, and ω_r is the rotor angular velocity. Combining Formulas (1) and (2) gives the synchronous mechanical rotor velocity

$$\omega_r = \frac{\omega_p + \omega_c}{p_p + p_c}. \tag{3}$$

The natural angular mechanical velocity of the rotor is

$$\omega_n = \frac{\omega_p}{p_p + p_c}. \tag{4}$$

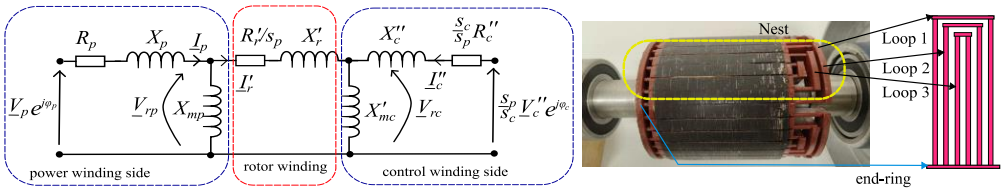

(a) (b)

Fig. 1. The SECM: (a) Circuit diagram with parameters referred to the power winding side (' – denotes reference from the rotor side, " – denotes reference from the control winding side); (b) nested-loop winding of the physical rotor. The equivalent parameters are R_p and X_p – power winding resistance and leakage reactance, X_{mp} and X_{mc} – magnetising reactances, R_c and X_c – control winding resistance and leakage reactance, and R_r and X_r are rotor winding resistance and reactance

Figure 2 illustrates the convention used to relate the three-phase quantities to the *dq* quantities. $\underline{V}_p$ and $\underline{V}_c$ represent the RMS phase voltages of the power and control windings, respectively. The voltages, currents, and equivalent parameters of the SECM are referenced to the power winding side, using the effective turns' ratios in Table 1. The effective turns ratio, in general, is the ratio of the magnitudes of the fundamental components of the air-gap magnetic flux density of the stator winding and the rotor winding, determined at unit currents [4, 14, 27].

Table 1. Referring parameters of SECM to the power winding side [4]

Referred quantity or lumped parameter	**Reference**
Power winding voltage and current	$V_p \cdot (1/1), \quad \underline{I}_p \cdot (1/1)$
Power winding resistance and leakage reactance	$R_p \cdot (1/1), \quad X_p \cdot (1/1)$
Power winding magnetising reactance	$X_{mp} \cdot (1/1)$
Control winding voltage and current	$V_c' = V_c \cdot n_r, \quad \underline{I}_c' = I_c / n_r$
Control winding resistance and leakage inductance	$R_c'' = R_c \cdot n_r^2, \quad X_c'' = X_c \cdot n_r^2$
Control winding magnetising reactance	$X_{mc}' = X_{mc} \cdot n_r^2$
Rotor winding current	$I_r' = I_r \cdot n_{rp}^{-1}$
The rotor winding resistance and leakage reactance	$R_r' = R_r \cdot n_{rp}^2, \quad X_r' = X_r \cdot n_{rp}^2$

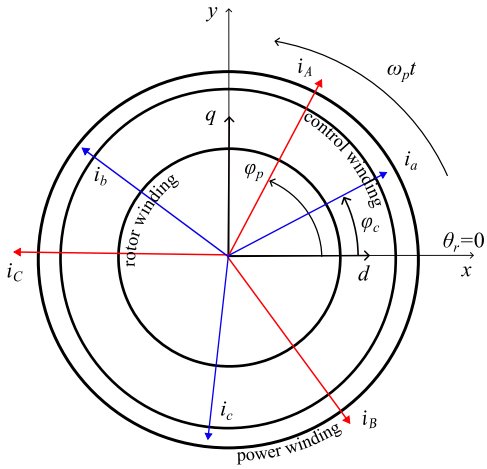

Fig. 2. Convention relating the three-phase and dq quantities; i_A, i_B, and i_C represent the power winding three-phase currents, while i_a, i_b, and i_c represent the control winding three-phase currents, and θ_r is the rotor angle. Transformations from phase to dq quantities for BDFIM are provided in [4,5]

The effective turns ratio from the control winding to the power winding, also referred to as the rotor turns ratio, is [5]

$$n_r = \frac{n_{rp}}{n_{rc}}, \tag{5}$$

where

$$n_{rp} \overset{\text{def}}{=} \frac{B_p\big|_{|I_p|=1A}}{B_{rp}\big|_{|I_r|=1A}}, \tag{6}$$

$$n_{rc} \overset{\text{def}}{=} \frac{B_c\big|_{|I_c|=1A}}{B_{rc}\big|_{|I_r|=1A}}. \tag{7}$$

B_p and B_c are the magnitudes of the fundamental components of the air-gap magnetic flux density developed by the power and the control winding, respectively. B_{rp} and B_{rc} are the components of air-gap magnetic flux density with pole-pair numbers p_p and p_c, respectively. Ratio (5) depends on the winding design in the stator and rotor, and an optimal value for this ratio exists, as noted in [6]. As demonstrated in [4], for the nested-loop rotor winding design, this ratio can only be approximately described by the analytical expression. The imposition of the unit rotor current on the rotor winding will be further explored. We will also indicate the inconsistency in the approach relying solely on Formulas (6)–(7).

Next, there are electrical angles φ_p and φ_c (see Fig. 2), which are related to mechanical angles η, θ_r, ψ in Fig. 3 in the following way:

$$\varphi_p = p_p\theta_r + p_p\eta, \tag{8}$$

$$\varphi_c = p_p\theta_r - \left(p_p + p_c\right)\theta_r + p_p\eta + p_c\psi, \tag{9}$$

where η represents the initial angular position of the rotor in the finite element model, and ψ is associated with the distribution of stator windings in a particular machine.

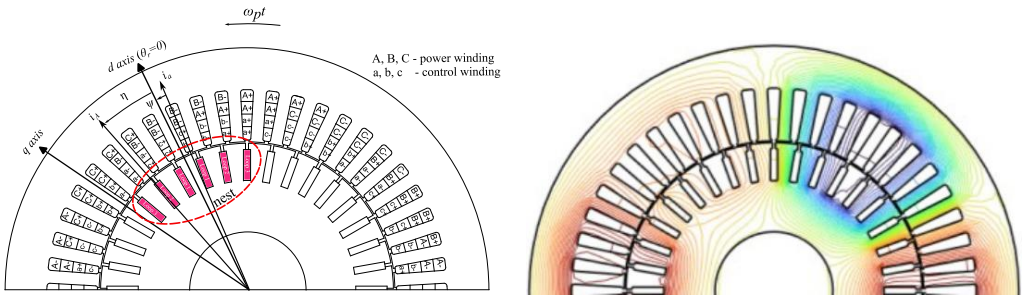

(a) (b)

Fig. 3. Cross-section of the BDFIM under study: (a) with stator and rotor windings distributions; (b) magnetic field distribution at natural velocity corresponding to $\omega_p t = 0$ and $\theta_r = 0$

The electromagnetic torque is calculated as [4, 5]

$$T_e = \left(1 - s_p\right) \frac{3P_p}{\omega_r} + \left(1 - s_c\right) \frac{3P_c}{\omega_r}, \tag{10}$$

where P_p and P_c are the active powers delivered to the rotor branch in Fig. 1 on the power and control winding sides, respectively.

2.2. Finite element models

The finite element model used to extract the SECM parameters is a nonlinear, steady-state, frequency-domain, complex-valued model developed in [25]. The 2-D time-domain problem was transformed into a frequency-domain problem using the rotor slips. The model employs a rigorous finite element formulation of the voltage-driven problem governed by the equation

$$-\text{div}\left(\nu_{\text{eff}}\left(\underline{\boldsymbol{B}}'\right)\textbf{grad}\,\underline{A}'\right) = \underline{J}_p + \underline{J}_c + \sigma\left(j s_p \omega_p \underline{A}' - \frac{\underline{u}'}{\text{l}}\right), \tag{11}$$

where $\underline{A}'$ is a modified complex magnetic vector potential representing the algebraic sum of the potentials associated with the fundamental time-harmonic of the rotating magnetic field developed by the current densities of the two stator windings: $\underline{J}_p$ of the power winding and $\underline{J}_c$ of the control winding. Similarly, the complex voltage $\underline{u}$ is the sum of voltages across the rotor bars, associated with these magnetic fields, and $\underline{\boldsymbol{B}}' = \textbf{curl}\,\underline{A}'$. The complex current densities $\underline{J}_p$ and $\underline{J}_c$ associated with the stator power and control winding, respectively, and the voltage $\underline{u}'$, are determined from the equations of the coupled circuits considering stator and rotor winding topological distributions. The effective magnetic reluctivity ν_{eff} is used to account for the saturation of steel as described in [25, 26]. To solve the SECM parameter extraction problem, the above model must be executed multiple times. It is convenient to consider this model as a THFEM (Time-harmonic Finite Element Model) procedure that takes input data and computes the output

$$\begin{bmatrix} \underline{I}_p \\ \underline{I}_c \\ T_e \end{bmatrix} = \text{THFEM}\begin{pmatrix} \text{machine geometry data,} \\ \text{BDFIM operating mode,} \\ \text{material data,} \\ V_p, V_c, \theta_r, \omega_p, \omega_c \end{pmatrix}, \tag{12}$$

where

$$T_e = \frac{r_a^2}{2\mu_0} \int_0^{2\pi} \Re \left\{ \underline{B}_r \underline{B}_\theta^* \right\} \mathrm{d}\theta \tag{13}$$

is the electromagnetic torque with r_a as the air-gap radius, $\underline{B}_r$ and $\underline{B}_\theta$ as the complex magnitudes of the radial and circumferential components of air-gap magnetic flux density, respectively. The parentheses in (11) enclose the input data, while the square brackets enclose the output data. An additional static model called further STAFEM (Magnetostatic Finite Element Model) must accompany this model. It implements a current-driven problem and can be described as follows:

$$-\mathrm{div}\left(\nu_{\mathrm{eff}}\, \mathbf{grad}\, A\right) = J_p + J_c + J_r, \tag{14}$$

$$\begin{bmatrix} n_{rp} \\ n_{rc} \\ X_p \\ X_c \\ X_{mp} \\ X_{mc} \end{bmatrix} = \mathrm{STAFEM}\left(\begin{array}{c} \text{machine geometry data} \\ J_p, J_c, J_r \\ \text{distribution of frozen permeability from THFEM} \end{array} \right), \tag{15}$$

where J_p, J_c are the real-valued current densities associated with the stator power and control winding, respectively, and J_r is the real-valued current density associated with the rotor winding. Model (13) does not compute a separate finite-element reluctance matrix; instead, it uses one computed by the THFEM. This technique, known as the frozen permeability method [28], enables the extraction of inductances while considering magnetic saturation. The current densities in (15) can be taken from either real or imaginary components of the complex values obtained from the THFEM.

3. Parameter extraction

3.1. Reference BDFIM

A summary of the reference physical BDFIM specification is presented in Table 2. Figure 3 displays the *dq* axes' location and the stator winding distributions over the machine cross-section. To ensure synchronisation between the THFFEM and SECM, the angles ϑ and ψ in (8)–(9) need to be determined based on the machine geometry, initial rotor angle, and stator windings distributions across the stator slots.

3.2. Methodology

First, the parameters to extract are the effective turn ratios. Using definitions (5)–(7), a unit current must be distributed over the rotor bars. It is assumed that the currents in all loops within each nest have the same phase angle and that their sum equals 1 A. We examined two methods for distributing the current through the rotor bars. Method 1 assumes that the current in each loop is equal to 1/3 A, while in Method 2, the currents are proportional to the effective area of the loop. For this machine, this reasoning yields the following current values: for Loop 1: $5/(1+3+5)$ A, for Loop : $3/(1+3+5)$ A, for Loop 3: $1/(1+3+5)$ A, as the ratio of effective areas for the

loops can be expressed by the ratio of their slot spans. The currents are distributed over the bars, assuming there is no phase shift between the currents of the loops within the same nest and that the currents circulate within the loops. The incorrect approach would be to enforce the current distributions composed of the two spatial harmonics p_p and p_c, which would violate the physical paths of the currents determined by the bar connections. Figure 4 displays these two distributions.

Table 2. Specification of the BDFIM under analysis

Parameter	Value
Stator frame diameter and axial length	210 mm and 105 mm
Number of stator pole-pairs	Power winding: $p_p = 2$, control winding: $p_c = 4$
Stator, rotor slot numbers	48, 36
Power winding nominal phase voltage, phase resistance, and end-winding reactance	230 V, 2.3 Ω, 2.0 Ω
Control winding nominal phase voltage, phase resistance, and end-winding reactance	230 V, 5.4 Ω, 3.1 Ω.
Rotor end-winding resistances and inductance	Loop 1: 115 μΩ, 0.07 μH Loop 2: 39 μΩ, 0.04 μH Loop 3: 27 μΩ, 0.01 μH
Rotor end-ring sector resistance:	4 μΩ, 0.02 μH

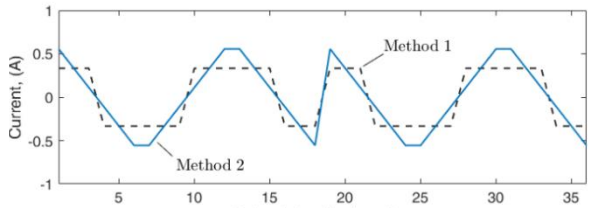

Fig. 4. Current distributions over rotor bars that correspond to the two methods

We initially ran the THFEM at ω_n in single-feed mode, reducing the power winding voltage to 75%of the nominal value. This was to ensure the measurements described later were taken under conditions that minimise core losses and temperature rise in the rotor winding during the experiment. In modelling, it was observed that increasing the voltage to 110% of the nominal value had virtually no impact on the extracted rotor parameters. We performed this step solely to determine the permeability distribution for the stator and rotor. Next, we ran a STAFEM twice, applying unit currents to either the stator or the rotor windings, and considering the rotor winding current distributions shown in Fig. 4. B_p, B_c, B_{rp}, B_{rc} in (5)–(7) were determined from the air-gap distributions of the radial components of magnetic flux density using FFT. The results are presented in Table 3.

Table 3. Computed values of the effective turns' ratios

Method	n_{rp}	n_{rc}	n_r
1	77.46	101.57	0.76
2	60.82	84.91	0.71

Later, the values in Table 3 will be examined for accuracy. Before proceeding, it is crucial to outline the methodology used to extract the remaining reactances. The leakage – X_p and X_c and the magnetising reactances X_{mp} and X_{mc} are extracted using the following relationships. Given the operating point, the THFEM was executed, and next the STAFEM was executed based on the permeability distribution from the THFEM. The stator reactances were determined by alternately feeding phases "A" and "a" with unit current, while the remaining phases and the rotor winding were left open. The leakage and magnetising reactances were calculated as [23].

$$X_p = \omega_p \left(|\lambda_A| - |\lambda_B| - |\lambda_C|\right) + X_{pe}, \tag{16}$$

$$X_c = \omega_p \left(|\lambda_a| - |\lambda_b| - |\lambda_c|\right) + X_{ce}, \tag{17}$$

where λ indexed by the phase label represents the phase magnetic flux and X_{pe}, X_{ce} the reactances of the stator end-windings of the power and control windings, respectively [24]. The magneting reactances were determined as follows:

$$X_{mp} = \frac{3}{2}\left(\omega_p \left|\lambda_A\right| - \left|X_p - X_{pe}\right|\right), \tag{18}$$

$$X_{mc} = \frac{3}{2}\left(\omega_p \left|\lambda_a\right| - \left|X_c - X_{ce}\right|\right). \tag{19}$$

The factor 3/2 is required due to the single-phase supply. The rotor winding parameters were extracted using the power balance equations, based on voltages and currents obtained from the THFEM. From Fig. 1, it can be deduced that for the active power delivered to the rotor winding equivalent terminals, the following equations apply [2,4,5]:

$$3 \cdot P_p + 3 \cdot P_c \overset{\text{def}}{=} 3 \cdot \left|\underline{I}'_r\right|^2 R'_r \frac{1}{s_p} + T_e \omega_r, \tag{20}$$

$$3 \cdot Q_p + 3 \cdot Q_c \overset{\text{def}}{=} 3 \cdot \left|\underline{I}'_r\right|^2 X'_r, \tag{21}$$

where the active powers are

$$P_p = \Re\left\{\underline{V}_{rp}\underline{I}'^{*}_r\right\}, \tag{22}$$

$$P_c = \frac{s_p}{s_c}\Re\left\{\underline{V}_{rc}\underline{I}'^{*}_r\right\}, \tag{23}$$

and the reactive powers are

$$Q_p = \Im\left\{\underline{V}_{rp}\underline{I}'^{*}_r\right\}, \tag{24}$$

$$Q_c = \frac{s_p}{s_c}\Im\left\{\underline{V}_{rc}\underline{I}'^{*}_r\right\}, \tag{25}$$

where

$$\underline{I}'_r = \underline{I}_p - \frac{\underline{V}_{rp}}{jX_{mp}} \quad \text{or} \quad \underline{I}'_r = \frac{\underline{V}_{rc}}{jX'_{mc}} - \underline{I}''_c. \tag{26}$$

All parameters of the SECM are now described, except for the resistances, which were measured (see Table 3). The parameter extraction requires that the THFEM and STAFEM be executed in a sequence, as shown in Fig. 5.

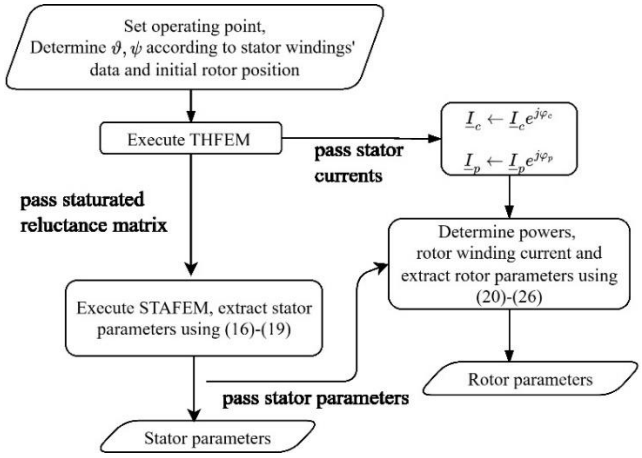

Fig. 5. Flowchart diagram illustrating the extraction of SECM parameters

4. Results

In Fig. 6, the results of a magnetisation test are presented for both stator windings. During laboratory tests, the machine was operated at synchronous velocity of the stator windings, with a proportional increase in voltage. The analysis using the THFEM assumed identical conditions. Figure 7 compares the cascade characteristics obtained using the THFEM, SECM

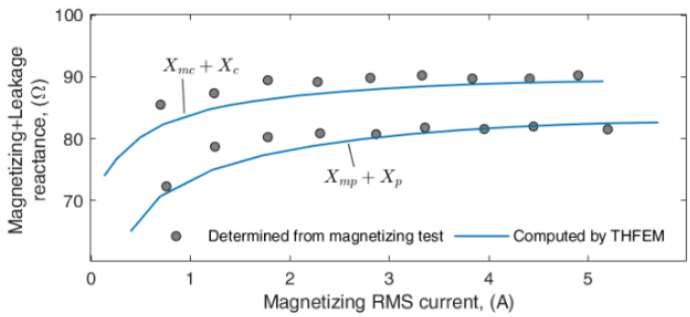

Fig. 6. Variations of series connections of leakage and magnetising reactances versus magnetising

and measurements at a 50 Hz supply. In method one (see Fig. 1(a)), the results less favourably correspond to those from the THFEM than in method two because the assumed rotor current distribution is more specific to winding designs with bars connected in series. In method two, the data obtained from the SECM closely resemble those of the THFEM, making it difficult to discern any discrepancies; the value of $n_r = 0.71$ in Table 3 appears correct. However, if n_r is constant, there is a difference between the rotor currents determined using both formulas in (26) that reaches 5% in relative values. This means that the inconsistency in rotor powers is even higher, suggesting that n_r cannot be accurately determined unless the equality constraint is imposed on the rotor current. It can be deduced from Fig. 1(a) and (26) that this constraint is equivalent to n_r determined as current for both stator windings.

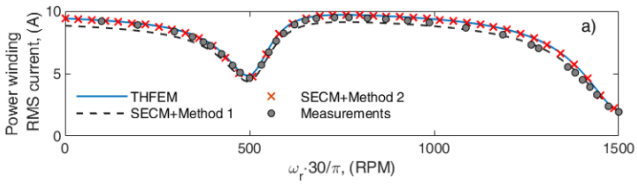

(a)

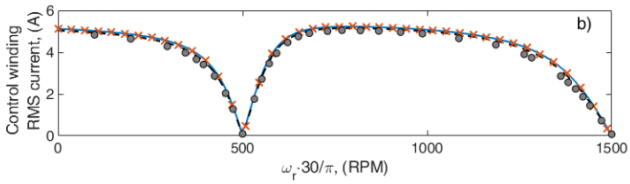

(b)

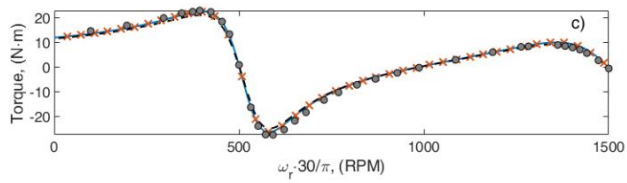

(c)

Fig. 7. Characteristics determined in cascade mode for $|\underline{V}_p| = 172$ V RMS: (a) RMS phase current of the power winding; (b) RMS phase current of the control winding, and (c) electromagnetic torque

$$n_r = \frac{\left|\dfrac{\underline{V}_{rc}}{jX_{mc}} - \underline{I}_c\right|}{\left|\underline{I}_p - \dfrac{\underline{V}_{rp}}{jX_{mp}}\right|}. \tag{27}$$

The variation of n_r versus rotor speed, determined from (27), is shown in Fig. 8. The observed frequency dependence is not substantial. However, it becomes crucial in fulfilling the power balance equations, (20) and (21). Formula (27) also suggests a method to enhance accuracy in experimental approaches, and that variation of n_r in the double-feed mode will differ from that in Fig. 8.

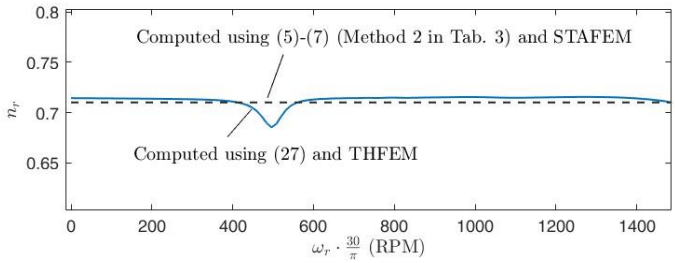

Fig. 8. Variation of the effective turns' ratio n_r determined from (27) compared with that determined according to Method 2 in Table 3, under the conditions in Fig. 7

The rotor parameters variations corresponding to the results in Fig. 7 are plotted in Fig. 9. The variation of R'_r due to skin effect is clearly exposed by the main trend. The parameters exhibit peaks at ω_n. To explain this phenomenon, from (20)–(25) and Table 2, one can deduce that at natural speed, when $T_e = 0$.

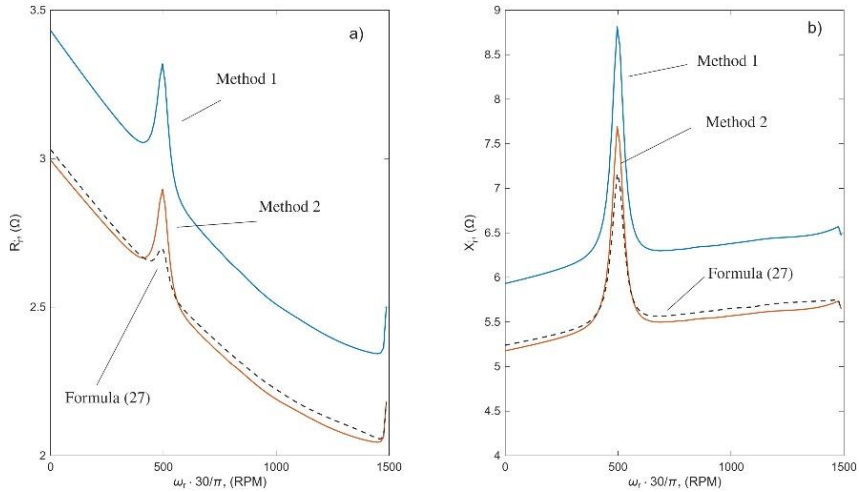

(a) (b)

Fig. 9. Variations of rotor equivalent parameters versus rotor speed corresponding to the results in Fig. 7: (a) equivalent referred resistance, and (b) equivalent referred reactance

$$R'_r\big|_{\omega_n} = s_p \Re\left\{\underline{V}_{rp} \frac{\underline{I}_r^*}{|\underline{I}_r|^2}\right\} n_{rp}, \tag{28}$$

$$X'_r\big|_{\omega_n} = \Im\left\{\underline{V}_{rp} \frac{\underline{I}_r^*}{|\underline{I}_r|^2}\right\} n_{rp} - X_{mc} n_r^2. \tag{29}$$

The referred parameters aggregate the variations of the non-referred parameters, the variations of effective turns' ratios n_{rp} and n_r, and those of the magnetising reactance.

Variations in rotor winding parameters with rotor speed were previously observed in [21]; however, they were considered relatively small and had a negligible impact on terminal quantities. In contrast, the variations identified in this study are more pronounced and warrant further explanation.

At the natural velocity, the relative motion between the rotor's spatial harmonics and the control winding field vanishes. In the absence of control winding current, the counter-electromotive force that typically suppresses differential leakage field harmonics (of orders $p_p \pm k\,(p_p + p_c)$ where $k >$ is a natural number) is effectively absent. Consequently, these harmonics – which couple solely with the rotor winding loops – allow their associated magnetic energy to manifest as a localised increase in the rotor's leakage inductance. It is crucial to emphasise that the magnitude of this phenomenon is closely tied to the specific slot combination (48/36) and the geometry of the nested-loop winding, which can amplify certain spatial orders of magnetic flux density. Ideally, a fully rigorous derivation would incorporate corresponding variations into the magnetising inductances, which could potentially mitigate this increase by aggregating in the variation of X_{mc} (see Eq. (29)). However, such an extension would introduce a level of complexity impractical for the proposed extraction procedure. This phenomenon also accounts for the observed rise in rotor resistance, as the same spatial harmonics affect the skin effect in the rotor bars.

The low impact of these variations on the terminal quantities can, in turn, be explained by an observation that, in the single-feed mode, the equivalent impedance of the two branches on the control winding side that can be expressed as

$$\underline{Z}_c'' = n_r^2 \cdot \left(\left(\frac{s_c}{s_p} R_c + jX_c \right) \parallel jX_{mc} \right), \tag{30}$$

where $\parallel$ stands for the parallel connection, which is connected in series with the rotor impedance.

Consider that, according to the results in Figs. 8 and 9(b), at rotor speeds equal to 400 rpm and 45 rpm, X_r' is equal to 5.25 W and 5.60 W, respectively, and n_r^2 to 0.71 and 0.69, respectively. Note that relative variation in X_r' is nearly the same as minus relative variation in $\underline{Z}_c''$. Thus, the rise in X_r' around ω_n is compensated by the drop in n_r^2 (see Figs. 8 and 9(b)). This reveals the self-compensating mechanism of rotor parameter variation in the SECM. Figure 10 provides experimental evidence supporting the existence of these parameter variations, determined by combining laboratory measurements with THFEM computations. For this analysis, the measured stator voltages, currents, power factor, and torque were utilised under conditions corresponding to Fig. 7, along with the previously extracted X_p, X_c, X_{mp}, X_{mc}. Stator temperature was monitored during the test, and the winding resistances were modified accordingly. The variations of n_r were calculated using (27), and subsequently, the referred rotor parameters were derived via (20)–(26). It is important to note that while the trend of parameter variations mirrors that observed in the FEM analysis (Figs. 8 and 9), the magnitudes of the peaks differ. This discrepancy is attributed to an inherent limitation of the experimental extraction procedure: it employs constant magnetising reactances determined from no-load tests, thereby neglecting the specific impact of differential harmonics on these reactances discussed earlier. Consequently, the experiment qualitatively validates the harmonic impact, although the quantitative values are subject to this approximation. Additionally, the rotor resistance determined at ω_n is higher than the extracted value, which accounts for core losses, stray load losses, and rotor temperature rise in the physical machine – factors not fully separated here.

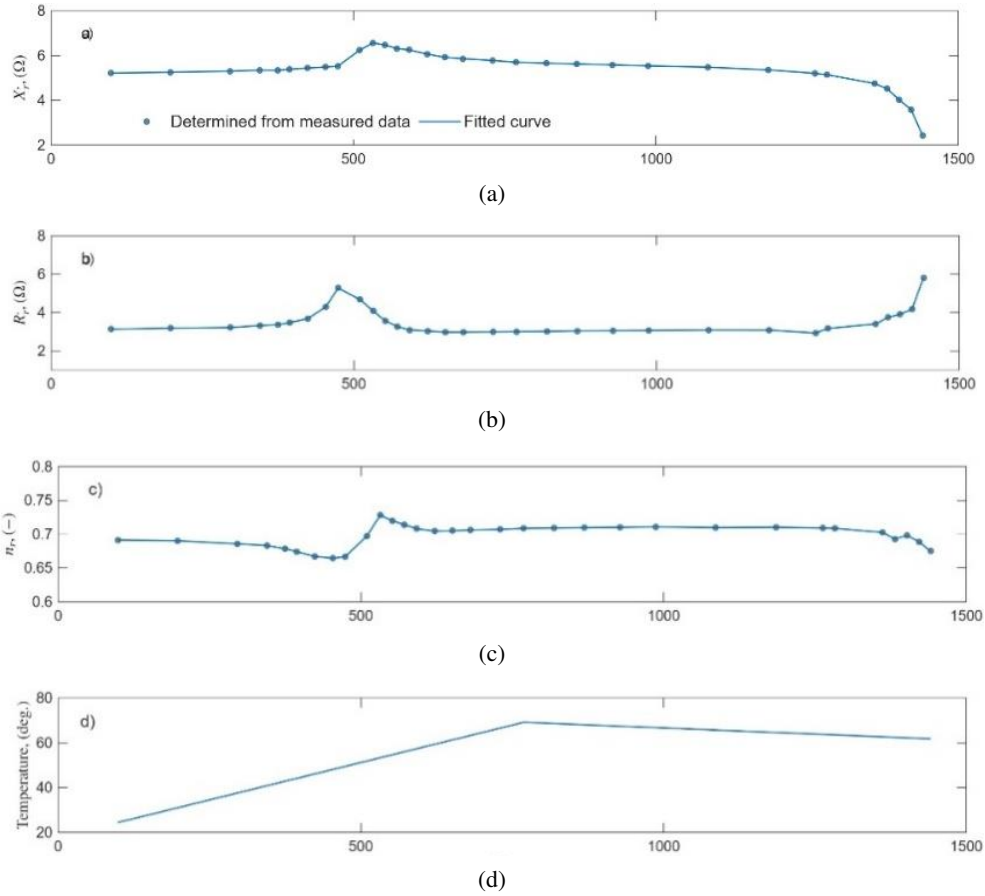

Fig. 10. Variations of parameters versus rotor speed determined from experimental data under the conditions in Fig. 7: (a) rotor winding referred reactance; (b) rotor winding referred resistance; (c) rotor effective turns ratio; (d) stator slot temperature

The variations in rotor parameters in the double-feed mode can be determined using the same procedure; however, not at the operating points where the powers or rotor currents are zero. Therefore, a common practice is to use the constant parameters estimated in single-feed mode in double-feed mode [21]. However, we are aware that the impact of differential harmonics flux depends on the control winding current, which varies widely during regular operation; therefore, the rotor parameters will vary accordingly. When the rotor parameters are constant, there will be no self-compensating effect described above, and the enforced consistency of rotor current. The question arises as to what extent it affects the results.

In Fig. 11, the analysis illustrates the variations in rotor parameters in the double-feed mode at a specific operating point. We selected the speed at which, given the power winding voltage, the rotor current reaches zero for some control winding voltage value. In Figs. 11(b)–11(d), the Fig. 5 procedure is used to extract the rotor parameters. The analysis carried out by varying φ_c

given $|\underline{V}_p|$ and $|\underline{V}_c|$. As can be seen, at some amplitude $|\underline{V}_c|$, the parameters cannot be determined because the rotor current approaches zero. Under these conditions, for the SECM we used the rotor parameters obtained by averaging the variations in Figs. 8–9 over the whole range of rotor velocity, to obtain $R'_r = 2.45\ \Omega$, $X'_r = 5.63\ \Omega$ and $n_r = 0.71$. To show the impact of n_r variation alone, the simulation is performed in Fig. 12(a)–12(b), assuming a 5% spread of the rotor parameters from the above values.

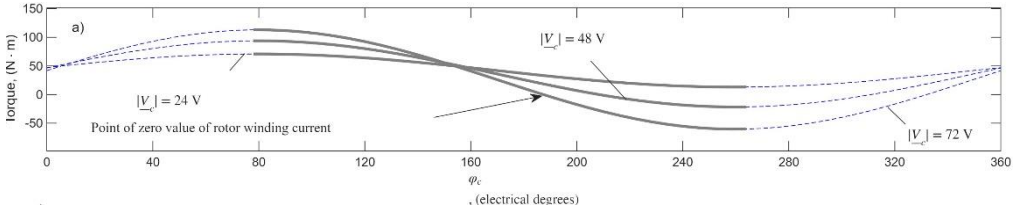

(a)

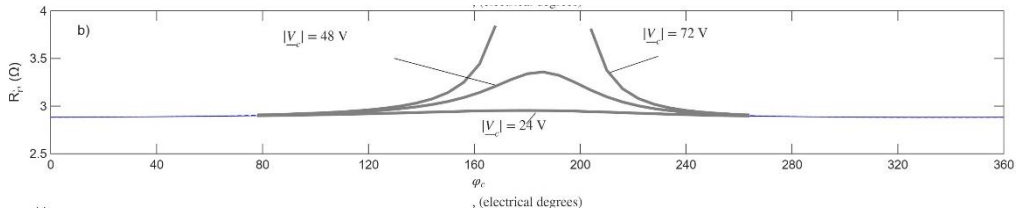

(b)

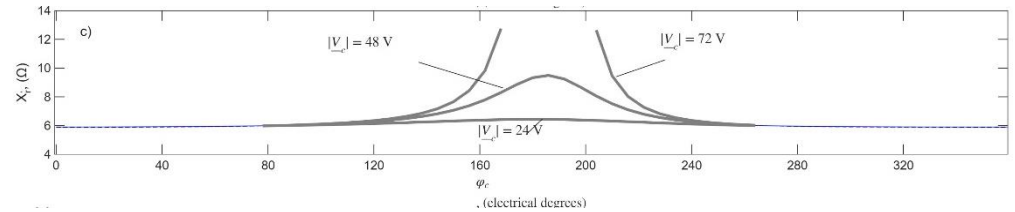

(c)

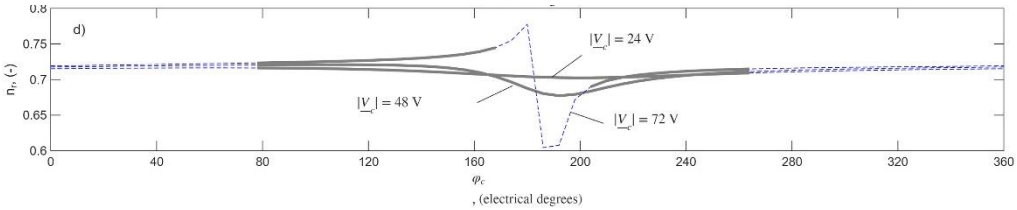

(d)

Fig. 11. Variations of electromagnetic torque and rotor winding parameters in double-feed mode for rotor speed equal to 400 RPM, $|\underline{V}_p| = 243$ V RMS and $|\underline{V}_c| = 24, 48, 72$ V RMS vs. control voltage phase angle; thick grey line denotes stable operating region: (a) electromagnetic torque; (b) referred rotor resistance; (c) referred rotor reactance; (d) effective rotor turns ratio

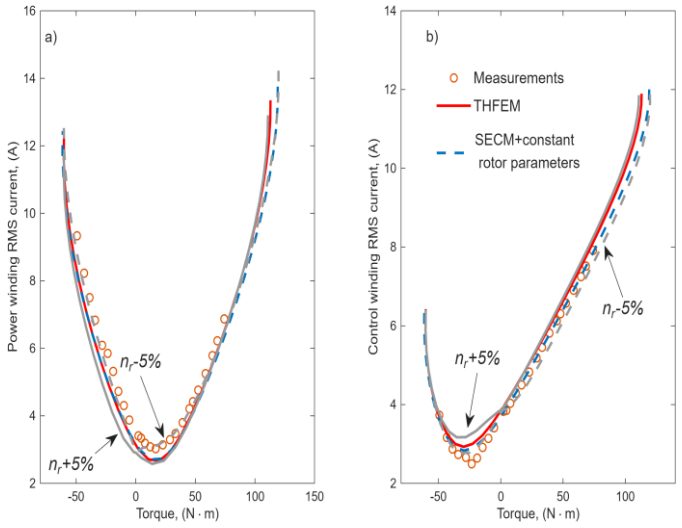

(a) (b)

Fig. 12. Variations of stator winding current vs. torque for different methods of computations compared with measured values for rotor speed equal to 400 RPM, $|\underline{V}_p|$ = 243 V RMS, $|\underline{V}_c|$ = 72 V RMS: (a) power winding RMS current; (b) control winding RMS current. Grey thick lines represent the SECM with constant parameters, where the n_r was varied by ±5% from the value of 0.71

The analysis of the results in Fig. 12 shows that:

i) In the high-torque range, the SECM with constant, well-estimated rotor parameters shows maximum differences of about 6% in torque and 15% in current relative to the THFEM predictions. In this operating range, the terminal currents are determined mostly by the rotor current. From (27), it can be deduced that a change in n_r mainly affects the rotor currents, not the magnetising currents. A decrease in n_r is equivalent to a decrease in the terminal current because a lower active component of the terminal current is required to produce the same torque, and vice versa, an increase in n_r increases this component. This shows that an incorrect estimation of n_r in the model leads to underestimation of the apparent power required by the machine from the inverter in relative values equal to or greater than the change in n_r.

ii) In the low-torque range, the SECM with constant well-estimated parameters resembles the accuracy of the THFEM. In this range, the terminal current is determined mostly by the magnetising current. The relatively low immunity of the terminal currents to the n_r parameter variation results from the low value of the currents, rather than from the variation of the current due to n_r alone.

For example, the sensitivity of the current $\left|\underline{I}_p\right| \approx I_{mp}$ defined after [29] as

$$S_{n_r}^{I_{mp}} = \frac{n_r}{I_{mp}} \frac{\partial I_{mp}}{\partial n_r} \tag{31}$$

is relatively high due to small I_{mp} although the first formula in Eq. (27) suggests $\dfrac{\partial I_{mp}}{\partial n_r}$ being very small. Ultimately, it should be emphasised that this analysis is conducted primarily from

a theoretical and phenomenological perspective to better understand the impact of rotor current inconsistencies. While it demonstrates that the constant-parameter SECM might benefit from adaptive estimation to maintain absolute precision, this is largely an observational insight. For the vast majority of practical engineering applications, the accuracy achieved by utilising averaged parameters derived from single-feed operation is entirely sufficient.

5. Conclusions

This paper establishes a direct link between the physical phenomena in a nested-loop rotor BDFIM- captured by the time-harmonic finite element model - and its equivalent constant-parameter circuit model. A parameter extraction methodology is proposed. The investigation demonstrates that a self-compensating mechanism minimises the impact of frequency-dependent rotor leakage reactance variations in single-feed operation, namely, when the rotor reactance increases, the effective turns ratio decreases. This variation was attributed to differential leakage fluxes trapped in the nested-loop winding when the control winding current is low. The study identifies a low-torque, low-power zone where inaccuracies in estimating the effective turns ratio can lead to noticeable differences, due to the model's increased sensitivity at low current. The research reconciles the computational and experimental domains, proposing a formula for accurately determining the effective turns ratio and clarifying that measurement techniques based on terminal quantities can mask the underlying physical variations confirmed by the finite-element model, thereby filtering them out. These findings are particularly representative of BDFIMs with nested-loop rotor structures and specific stator-to-rotor slot number ratios. For other rotor winding designs or different slot combinations, the observed parameter variations may be less pronounced. Thus, the analysis presented here serves as a cautionary note rather than a universal rule.

Acknowledgments

The authors are grateful to colleagues at Warwick University in the United Kingdom for enabling the use of the specifications and measurements for the BDFIM in this study.

References

[1] McMahon R.A., Roberts P.C., Wang X., Tavner P.J., *Performance of BDFM as generator and motor*, IEE Proceedings Electric Power Applications, vol. 153, no. 2, pp. 289–299 (2006), DOI: 10.1049/ip-epa:20050289.

[2] Roberts P.C., McMahon R.A., Tavner P.J., Maciejowski J.M., Flack T.J., *Equivalent circuit for the brushless doubly-fed machine (BDFM) including parameter estimation and experimental verification*, IEE Proceedings – Electric Power Applications, vol. 152, no. 4, pp. 933–942 (2005), DOI: 10.1049/ip-epa:2004510.

[3] McMahon R.A., Wang X., Abdi-Jalebi E., Tavner P.J., Roberts P.C., Jagiela M., *The BDFM as a generator in wind turbines*, Proceedings of the 12th Int. Power Electronics and Motion Control Conference, Portoroz, Slovenia, pp. 1859–1865 (2006), DOI: 10.1109/EPEPEMC.2006.4778676.

[4] Roberts P.C., *A study of brushless doubly-fed (induction) machines*, PhD Thesis, University of Cambridge, Cambridge, United Kingdom (2005).

[5] Abdi E., *Modelling and instrumentation of brushless doubly-fed (induction) machines*, PhD Thesis, University of Cambridge, Cambridge, United Kingdom (2006).

[6] Wang X., Strous T.D., Lahaye D., Polinder H, Ferreira J.A., *Modeling and optimization of brushless doubly-fed induction machines using computationally efficient finite element analysis*, IEEE Transactions on Industry Applications, vol. 52, no. 6, pp. 4525–4534 (2016), DOI: 10.1109/TIA.2016.2593715.

[7] Strous T.D., *Brushless Doubly-Fed Induction Machines for Wind Turbine Drive-Train Applications*, PhD Thesis, Delft University of Technology, Delft, Netherlands (2016).

[8] Strous T.D., Polinder H., Ferreira J.A., *Brushless doubly-fed induction machines for wind turbines: developments and research challenges*, IET Electric Power Applications, vol. 11, no. 6, pp. 991–1000 (2017), DOI: 10.1049/iet-epa.2016.0118.

[9] Oreoluwa O., Nkosinathi G., *A review of the advancements in the design of brushless doubly fed machines*, Energies, MDPI, vol. 15, no. 725, pp. 2–19 (2022), DOI: 10.3390/en15030725.

[10] Shao S., Abdi E., Barati F., McMahon R.A., *Stator-flux-oriented vector control for brushless doubly-fed induction generator*, IEEE Transactions on Industrial Electronics, vol. 56, no. 10, pp. 4220–4228 (2009), DOI: 10.1109/TIE.2009.2024660.

[11] Hesar H.M., Liang X., Salahmanesh M.A, Khoshhava M.A., Abdi S., *Vector Control of Brushless Doubly-Fed Induction Machines Based on Highly Efficient Nonlinear Controllers*, IEEE Transactions on Industrial Electronics, vol. 71, no. 6, pp. 5641–5652 (2024), DOI: 10.1109/TIE.2023.3296811.

[12] Tohidi S., *Analysis and simplified modeling of brushless doubly-fed induction machine in synchronous mode of operation*, IET Electric Power Applications, vol. 10, no. 2, pp. 110–116 (2016), DOI: 10.1049/iet-epa.2015.0217.

[13] Gorti B.V., Alexander G.C., Spee R., *Power balance considerations for brushless doubly-fed machines*, IEEE Transactions on Energy Conversion, vol. 11, no. 4, pp. 687–692 (1996), DOI: 10.1109/60.556363.

[14] Yu K., Tag P., *Novel Equivalent Circuit Model and Theoretical Analysis of Doubly Fed Machine*, IEEE Transactions on Energy Conversion, vol. 34, no. 2, pp. 1073–1081 (2018), DOI: 10.1109/TEC.2018.2870867.

[15] Ge J., Xu W., Liu Y., Xiong F., *Novel Equivalent Circuit Model applicable to all operation modes for brushless doubly fed induction machines*, IEEE Transactions on Industrial Electronics, vol. 69, no. 12, pp. 12540–12550 (2022), DOI: 10.1109/TIE.2022.3144567.

[16] Mohammad Naser Hashemnia, Farzad Tahami, Peter Tavner, Sajjad Tohidi, *Steady-state analysis and performance of a brushless doubly fed machine accounting for core loss*, IET Electr. Power Applications, vol. 7, no. 3, pp. 170–178 (2013), DOI: 10.1049/iet-epa.2012.0215.

[17] Hashemnia M.N., Tahami F., Oyarbide E., *Investigation of Core Loss Effect on Steady-State Characteristics of Inverter Fed Brushless Doubly Fed Machines*, IEEE Transactions on Energy Conversion, vol. 29, no. 1, pp. 57–64 (2014), DOI: 10.1109/TEC.2013.2290428.

[18] Mosaddegh-Hesar H., Liang X., Salahmanesh M.-A., Abdi S., McMahon R., *Electrical Equivalent Circuit Models for Brushless Doubly-Fed Induction Machines: A Review*, IEEE Transactions on Transportation Electrification, vol. 11, no. 1, pp. 1603–1616 (2025), DOI: 10.1109/TTE.2024.3408112.

[19] Abdi S., Abdi E., Orayee A., McMahon R.A., *Equivalent circuit parameters for large brushless doubly fed machines (BDFMs)*, IEEE Transactions on Energy Conversion, vol. 29, no. 3, pp. 706–715 (2014), DOI: 10.1109/TEC.2014.2311736.

[20] McMahon R., Tavner P., Abdi E., Malliband P., Barker D., *Characterising brushless doubly fed machine rotors*, IET Electric Power Applications, vol. 7, no. 7, pp. 535–543 (2013), DOI: 10.1049/iet-epa.2012.0238.

[21] McMahon R., Roberts P., Tatlow M., Abdi E., Broekhof A., Abdi S., *Rotor parameter determination for the brushless doubly fed (induction) machine*, IET Electric Power Applications, vol. 9, no. 8, pp. 549–555 (2015), DOI: https://doi.org/10.1049/iet-epa.2015.0023.

[22] Abdi E., Abdi S., *Simplified Experimental Estimation of Equivalent Circuit Parameters for Brushless Doubly Fed Machines*, Proc of 49th IEEE Industrial Electronics Society Conference IECON, Singapore (2023), DOI: 10.1109/IECON51785.2023.10311914.

[23] Dolinar D., De Werdt R., Bellmans R., Freeman E.M., *Calculation of two-axis induction motor model parameters using finite elements*, IEEE Transactions on Magnetics, vol. 12, no. 2, pp. 133–42 (1997), DOI: 10.1109/60.629695.

[24] Boglietti A., Cavagnino A., Lazzari M., *Computational Algorithms for Induction-Motor Equivalent Circuit Parameter Determination – Part I: Resistances and Leakage Reactances*, IEEE Transactions on Industrial Electronics, vol. 58, pp. 3723–3733 (2011), DOI: 10.1109/TIE.2010.2084974.

[25] Jagieła M., Wang X., McMahon R.A., *Time-harmonic field-circuit model for brushless doubly fed induction machine*, IET Electric Power Applications, vol. 17, no. 7, pp. 965–975 (2023), DOI: 10.1049/elp2.12317.

[26] Jagieła M., Łukaniszyn M., *Time-harmonic field-circuit model for brushless doubly fed induction machine in natural operating mode*, Archives of Electrical Engineering, vol. 73, no. 3, pp. 615–628 (2024), DOI: 10.24425/aee.2024.150886.

[27] Pyrhonen J., Jokinen T., Hrabovcova V., *Design of rotating electrical machines*, Willey, Hoboken, New Jersey, USA (2007).

[28] Chu W.Q., Zhu Z.Q., *Average Torque Separation in Permanent Magnet Synchronous Machines Using Frozen Permeability*, IEEE Trans. on Magn., vol. 49, no. 3, pp. 1202–1210 (2013), DOI: 10.1109/TMAG.2012.2225068.

[29] Leon O.C., Desoer C.A, Kuh E.S., *Linear and nonlinear circuits*, Mc Graw -Hill, USA (1987).